Vertical Distribution Characteristics and Formation/Dissipation Mechanisms of Air Pollutants in Xingtai, China Based on Multi-source Data: A Case Study

Qi Jiang [1,2] • Fei Wang [3] • Zhanqing Li [4] • Yuan You [1,2] • Yuchen Jin [5] • Siteng Li [2,6], Yele Sun [7] • Yingjie Zhang [8] • Xinrong Ren [4,9] • Hao He [4] • Russell R. Dickerson[4]

Received: DD Month YEAR/ Accepted: DD Month YEAR/ Published online: DD Month YEAR

✉ Fei Wang
feiwang@cma.gov.cn
1. National Meteorological Centre, Beijing 100081, China;
2. Key Laboratory of Urban Meteorology, China Meteorological Administration, Beijing 100089, China;
3. CMA Key Laboratory of Cloud-Precipitation Physics and Weather Modification (CPML), CMA Weather Modification Centre (WMC), Beijing 100081, China;
4. Department of Atmospheric and Oceanic Science, University of Maryland, College Park, MD 20742, USA;
5. Inner Mongolia Institute of Meteorological Sciences, Hohhot 010051, China;
6. Institute of Urban Meteorology, Beijing 100089, China;
7. State Key Laboratory of Atmospheric Boundary Layer Physics and Atmospheric Chemistry, Institute of Atmospheric Physics, Chinese Academy of Sciences, Beijing 100029, China;
8. School of Ecology and Nature Conservation, Beijing Forestry University, Beijing 100083, China;
9. Air Resources Laboratory, National Oceanic and Atmospheric Administration, College Park, MD 20740, USA.

Abstract

The Beijing-Tianjin-Hebei urban agglomeration is one of the regions in China with the most severe air pollution. Using aircraft observations collected over Xingtai in May 2016 and multi-source data, such as aerosol chemical composition and lidar data, we analyzed aerosol composition and optical properties, vertical pollution characteristics of gases within the boundary layer, and their interactions with meteorological parameters. This study focuses on investigating the transport and evolution mechanisms of pollutants during transitions from polluted research flight No.7(RF7) to clean (RF8) periods in summertime Xingtai. Results show that during RF7, the near-surface submicron aerosol (PM_1) mass concentration was generally low (37.5 μg m^{-3}), with the contribution of inorganic salts far exceeding that of organic matter. During RF8, the near-surface wind speed slightly increased, and the dominant wind direction remained southeasterly. Vertically, pollutant concentrations showed notable decreasing trends, and the average near-surface PM_1 mass concentration slightly decreased (30.6 μg m^{-3}). However, the chemical components of PM_1 differed substantially from those during RF7. Aircraft observations indicated weak cold-air activities above 1000 m during RF8, while the southeasterly wind still prevailed below 1000 m, with a slight increase in wind speed. From RF7 to RF8, the overall vertical atmosphere gradually transitioned from polluted to clean conditions. During RF8, an inversion layer appeared in the temperature profile between 1100 m and 1300 m, with ~21.3% of this inversion coming from black carbon heating. During RF7, sulfur dioxide (SO_2), nitrogen dioxide (NO_2), and carbon monoxide (CO) were strongly correlated with the scattering coefficient, with correlation coefficients of 0.92 and 0.96 for SO_2 and NO_2, respectively. By contrast, during RF8, the correlations between SO_2, NO_2, and CO and the scattering coefficient decreased, with SO_2 having the highest correlation with the scattering coefficient (coefficient of determination = 0.88). From RF7 to RF8, the concentrations of various pollutants within the boundary layer, except for ozone (O_3), had decreasing trends. When the relative humidity was below 50%, O_3 generally contributed positively to extinction. There was no pronounced correlation between O_3 and relative humidity when the relative humidity exceeded 50%.

Keywords Boundary layer · Pollutants · Vertical observations · Chemical composition · Meteorological factors

1 Introduction

The planetary boundary layer (PBL) serves as a pivotal hub for the exchange of energy, water vapor, and matter between the surface and the atmosphere. In the PBL, physical quantities, such as wind, temperature, humidity, pressure, and turbulent diffusion, as well as chemical properties related to pollutant compositions and transformation mechanisms, vary dramatically in time and space, particularly in the vertical direction [Haskins et al., 2019; Jiang et al., 2021; Riedel et al., 2013; Sun et al., 2016b, 2020]. The formation and dissipation of atmospheric pollutants primarily occur within the PBL [Qu et al., 2017]. The physicochemical properties and evolution mechanisms of pollutants in the vertical direction remain crucial factors affecting the accuracy of air quality forecasting models [Brook et al., 2013]. Due to limitations in observation platforms and instrument resolution, existing studies on atmospheric pollution have primarily focused on ground-level measurements. It is still a complex and hot topic as to how the physical and chemical properties of the urban boundary layer interact with each other to jointly drive the formation, accumulation, and dissipation of atmospheric pollutants.

Vertical observation methods for atmospheric pollutants include comparisons of observations at different altitudes [Levin et al., 2009], meteorological tower observations (such as observations made at the Beijing 325-m Meteorological Tower [Wang et al., 2018]), sounding balloon or tethered balloon observations [Han et al., 2018], ground-based radar observations [Wang et al., 2012], aircraft measurements [Wang et al., 2024], and model simulations [Wu et al., 2011]. Each of these approaches can provide valuable insights into the vertical distribution and evolution of pollutants within the PBL. Friedrich et al. [2012] found that considering the liquid-water mixing ratio derived from the vertical humidity profile under moist-adiabatic conditions can provide a more precise determination of atmospheric stability. Zhou et al. [2018] utilized multi-source observations and numerical models to study the Yangtze River Delta region, revealing that the lifting of a cold front and the transport of pollutants facilitate the accumulation of pollutants at altitudes above 100 m rather than near the surface. Based on aircraft observations, Dong et al. [2017] demonstrated that surface cooling effects and the uneven changes in heating rates caused by absorbing aerosols altered the atmospheric temperature profile, resulting in increased stability within the PBL and instability above the PBL. The

vertical variation characteristics of pollutants within the urban boundary layer are closely related to the dynamic/thermodynamic structure and turbulence characteristics of the PBL. Pollutants do not simply decrease with altitude, e.g., aerosol mass concentrations under clean weather conditions decrease rapidly with altitude, whereas in polluted or stagnant weather conditions, aerosol concentrations gradually decrease with altitude [Ding et al., 2005]. The proportion of secondary organic carbon increases with altitude, as reported by Ren et al. [2021]. Simulation studies focused on the Beijing region have indicated that local sources contribute greatly to near-surface pollutants, with local contributions of nitrogen dioxide (NO_2), sulfur dioxide (SO_2), and the mass concentration of particulate matter with diameters less than 10 μm (PM_{10}) reaching up to 90%, 65% and 75%, respectively. However, at an altitude of 1.1 km, the contributions from external sources (e.g., cities south of Beijing) to SO_2 and PM_{10} exceed 50% [Wu et al., 2011]. Studies on air pollution in Beijing have suggested that the proportion of organic matter is the highest near the surface due to surface emissions. Under polluted conditions, aerosols are dominated by nitrates above 200 m [Sun et al., 2020]. At night, O_3 concentrations are higher in the upper boundary layer, where the hydrolysis of dinitrogen pentoxide (N_2O_5) to form nitrates becomes more significant. The formed nitrates contribute to increased ground-level nitrate concentrations the following day as the boundary layer mixes and develops [Sun et al., 2018].

The Beijing-Tianjin-Hebei region is located in the transition zone between mountainous and plain regions. Due to the joint effects of blocking systems and the unique topography, the atmospheric environment in this region highly sensitive and vulnerable [Xu et al., 2021], making it one of the regions with the most severe atmospheric pollution in China [Cai et al., 2020]. Xingtai, situated in southern Hebei Province, China, has a complex emission environment and high-intensity pollution emissions, making it a hotspot of air pollution in the Beijing-Tianjin-Hebei region. Air pollution is the result of the combined and interacting effects of multiple boundary-layer factors [Ren et al., 2021].

Although previous studies have enhanced our understanding of the boundary layer structure and pollution mechanisms in the Beijing-Tianjin-Hebei urban agglomeration, further analysis and discussion of related issues are still needed to overcome some limitations. Specifically, there is a lack of detailed spatiotemporal observations of the

boundary-layer structure, with most studies relying on low-resolution observations. Moreover, the boundary-layer structure is highly complex, with substantial differences under varying pollution conditions across different regions, thus requiring more extensive data support. In this study, we utilize aircraft observations, in conjunction with near-surface multi-source data, including submicron aerosol (PM_1) chemical composition, to analyze the physicochemical and optical properties of aerosols, characteristics of the vertical variation of pollution gases in the boundary layer and their interactions with meteorological parameters. Furthermore, we focus on the transport and evolution mechanisms of a pollution-to-clean process in Xingtai during the summer, aiming to provide insights into the dynamic processes that occur during such transitions.

The remainder of this paper is organized as follows. Section 2 describes the sites and campaigns. Section 3 analyzes the results. Finally, section 4 presents the main conclusions.

2 Sites and campaigns

To observe vertical profiles of aerosols and gases in the North China Plain, the Air Chemistry Research in Asia campaign was conducted in Hebei Province, east of the Taihang Mountains in the North China Plain, from May to June of 2016. During the campaign, 11 vertical observation experiments were carried out using the Y-12 aircraft flying out of four local airports. The Y-12 aircraft was equipped with various instruments to measure aerosol optical properties, gas concentrations, and meteorological data. Specifically, the 550-nm aerosol scattering coefficient was measured using an integrating nephelometer (model 3565, TSI Inc.) at three wavelengths with a temporal resolution of one second. The 550-nm absorption coefficient was measured by using a particle soot absorption photometer (Radiance Research Inc., USA) with a temporal resolution of one minute. The extinction coefficient is defined as the sum of the absorption and scattering coefficients. Wang et al. [2018, 2024] and Benish et al. [2020] provide detailed information about the observational instruments used in this experiment and flight trajectories. In the Xingtai region, a total of five flight experiments were conducted, referred to as RF1, RF6, RF7, RF8, and RF11. Fig.1 shows the flight trajectories of these experiments.

On 28 May 2016, two aircraft observation missions were conducted over the Xingtai region, one at ~0300 Coordinated Universal Time (UTC, experiment RF7, 11 am local time) and the other at 0900 UTC (experiment RF8, 5 pm local time). Sky conditions, as photographed by onboard observers, were different during each observation period (Fig. 2). During the RF7 flight, the sky at an altitude of 3 km appeared grayish-yellow, with low horizontal visibility. By contrast, during the RF8 flight, the horizontal visibility at high altitudes dramatically improved, and the sky appeared bright blue.

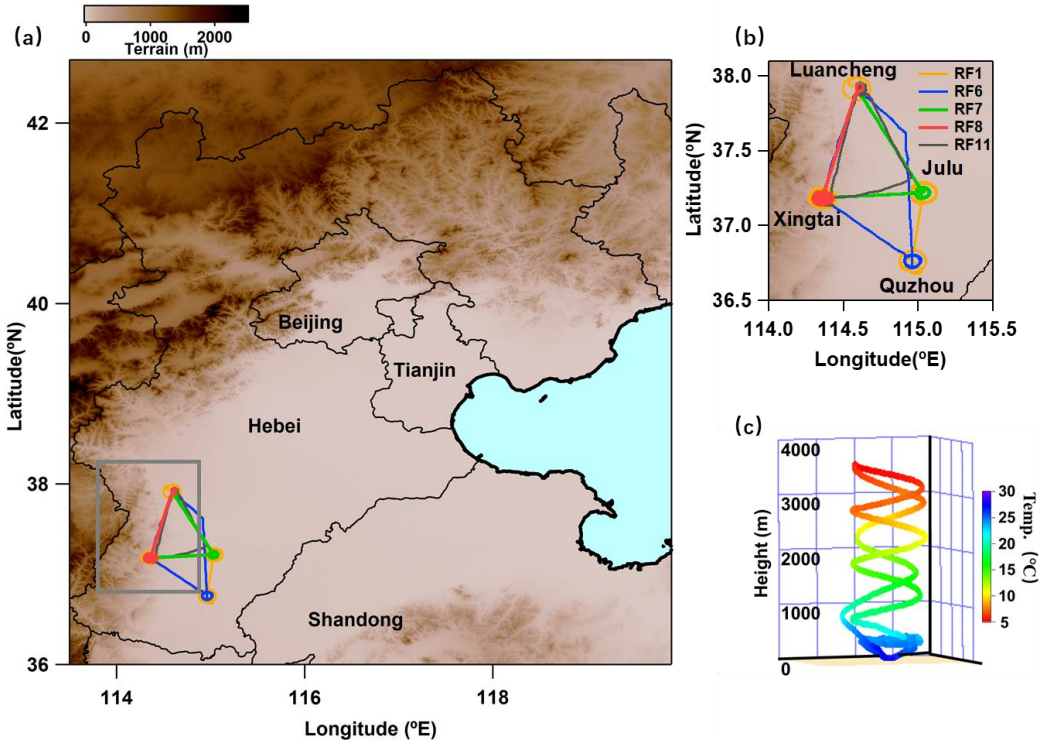

Fig. 1. (a) Five flight trajectories over Xingtai (colored lines) with terrain elevation (in m) as the background, (b) a zoomed-in view of the flight trajectories showing the locations of the airports that the aircraft flew from, and (c) vertical legs of each flight colored by the corresponding ambient air temperature.

Fig. 2. Aerial photographs taken during the RF7 and RF8 flights.

In conjunction with aircraft observations, various ground-based observations, including aerosol chemical composition and meteorological parameters, were simultaneously measured at the Xingtai supersite (114.36°E, 37.18°N; 182 m above sea level). Specifically, the chemical components of non-refractory PM_1 (NR-PM_1), including sulfate (SO_4^{2-}), nitrate (NO_3^-), ammonium (NH_4^+), chloride (Cl^-), and organics (Org), were measured in situ using an Aerodyne Aerosol Chemical Speciation Monitor (ACSM) at temporal resolutions of 5–8 minutes [Jiang et al., 2014; Sun et al., 2020b; Zhang et al., 2018]. Near-surface black carbon (BC) measurements were conducted using a seven-wavelength Aethalometer (model AE33, Magee Scientific, USA) [Drinovec et al., 2015; Wang et al., 2018]. The BC data used in this study were measured specifically at the 880-nm wavelength. Additionally, a MPL (Sigma Space Corporation, USA) was deployed at the Xingtai supersite. Particle number concentrations were measured using a scanning mobility particle sizer (model 3081/3085) with a resolution of five minutes. Ground-based extinction coefficients of particulate matter were obtained from a Cavity Attenuated Phase Shift-based extinction monitor. In addition, wind profiler radar data (114.65°E, 36.45°N; 58 m above sea level) with a temporal resolution of six minutes were provided by the Meteorological Observation Center of the China Meteorological Administration, offering parameters such as horizontal wind speed, wind direction, and vertical velocity.

3 Results

3.1 Ground-based observations

Figure 3 presents PM_1 and its chemical components (SO_4^{2-}, NO_3^-, NH_4^+, Cl^-, organic matter, and BC), ground-level organic sources derived from the source apportionment of organic matter, meteorological elements, particle number concentrations, and the vertical backscattering coefficient obtained from the MPL on 28 May 2016. The vertical atmospheric evolution of pollutants on that day can be divided into four distinct stages, denoted as S1, S2, S3, and S4. The RF7 and RF8 flight observations occurred during stages S1 and S2, respectively. Based on MPL observations from the Xingtai supersite, we analyzed the PBL heights (PBLHs) retrieved from the normalized relative backscatter using the wavelet covariance transform method [Gamage and Hagelberg, 1993] after eliminating the effects of clouds. The step size and threshold were set to 210 m and 0.05,

respectively. The first value from the lower layer exceeding this threshold or falling within a given threshold interval is considered to be the micropulse lidar-derived PBLH. Li et al. [2018] provide more details.

During stage S1, the surface wind was dominated by southeasterly wind, and the PBLH gradually increased. Near the surface up to an altitude of 500 m, radar echoes were relatively strong, indicating notable pollutant accumulation. However, ground-level PM_1 mass concentrations remained relatively low at 37.5 μg m^{-3}. The contribution of inorganic salts (NO_3^- + SO_4^{2-} + Cl^-) to PM_1 was considerably higher than that of organic matter, especially nitrates, which accounted for ~28% of the total PM_1 composition on average. In general, high temperatures and an elevated PBLH facilitate nitrate volatilization and concentration diffusion during the daytime, especially in summer, when nitrate concentrations begin to decrease markedly after sunrise. However, a noticeable peak in nitrate mass concentration was observed around 0200 UTC (10 am local time) on 28 May, surpassing the concentration of organic components. Importantly, there were no notable changes in wind direction and speed during this period, suggesting that the horizontal transport conditions of pollutants remained relatively stable. Studies on airship observations [Sun et al., 2018] and aircraft measurements [Pusede et al., 2016] have shown that regardless of pollution levels, the incremental contribution of nitrates above 200 m and higher altitudes is quite high during the nighttime. This is primarily attributed to the hydrolysis of N_2O_5 (formed from the reaction between high concentrations of NO_2 and O_3) in the upper boundary layer at night, generating substantial amounts of nitrates. Around sunrise, especially from 0100 to 0200 UTC, when boundary layer activities become more vigorous, the mixing effect becomes pronounced within the boundary layer, bringing high-concentration nitrates in the upper boundary layer down to near the surface, thereby resulting in a marked rise in the ground-level nitrate concentration. Therefore, the peak in the ground-level nitrate concentration around 0200 UTC was likely primarily due to the nitrates generated by the hydrolysis of N_2O_5 in the upper boundary layer during the previous night.

Using the positive matrix factorization method (Zhang et al., 2018), three types of organic aerosols were identified: two primary organic aerosols and one secondary organic aerosol, namely, hydrocarbon-like organic aerosol, cooking-related organic aerosol and oxygenated

organic aerosol. During stage S1, the oxygenated organic aerosol concentration gradually increased, and the proportion of secondary organic aerosol was over 65% of the organic matter on average, with an increasing trend. During this stage, one flight mission (RF7) with two vertical spirals (RF7a and RF7b) was conducted.

During stage S2, the near-surface wind speed increased slightly, and the wind direction fluctuated, but the prevailing wind direction remained southeasterly. Micropulse lidar (MPL) observations indicate that the thickness of the pollution layer decreased substantially during stage S2, with a clear reduction in pollutant concentration in the vertical direction. Although the average ground-level PM_1 mass concentration (30.6 μg m^{-3}) decreased slightly, the overall downward trend was not pronounced. However, the PM_1 chemical composition in stage S2 differed dramatically from that in stage S1. Notably, the contribution of nitrates decreased markedly during stage S2 (16%), while the proportion of organic matter increased notably, which became the dominant component of PM_1 (40%). Furthermore, the share of secondary organic aerosol in organic matter increased even more, contributing over 90%. During this stage, one flight mission (RF8) with three sub-missions (RF8a, RF8b, and RF8c) was conducted.

Upon entering stage S3, surface humidity gradually increased, and micropulse-lidar-derived radar echoes began to strengthen progressively in the vertical direction. Concurrently, the near-surface PM_1 mass concentration also rose notably. In particular, the mass concentration of organic matter increased from below 15 μg m^{-3} to 40 μg m^{-3} within two hours, with a growth rate exceeding 13 μg m^{-3}. Studies have shown that [Sun et al., 2016a, b; Wang et al., 2018] as pollution intensifies, the proportion of inorganic salts tends to increase remarkably, while the contribution of organic matter decreases. However, during stage S3, although the mass concentration of inorganic matter increased with increasing pollution, its growth rate was much lower than that of organic matter, with the average contribution of organic matter exceeding 48% of PM_1. According to the source apportionment results of organic matter during this period from Zhang et al. [2018], the mass concentration of cooking-related organic aerosols began to increase considerably around 1000 UTC, reaching a peak at 1200 UTC, coinciding with the local dinner cooking time in Xingtai. The rapidly increasing cooking-related organic aerosols contributed greatly to organic matter, with a proportion of up to 40%. During this time, cooking-related

organic aerosols played a crucial role in the occurrence and development of pollution in stage S3.

After entering stage S4, the wind direction shifted to the west, and the wind speed decreased markedly. In addition, the near-surface relative humidity remained around 70%, and the ground-level PM_1 mass concentration was slightly lower compared with stage S3, but the proportion of inorganic salts, particularly nitrates, increased rapidly. In terms of mass concentration variations, after nightfall, the mass concentrations of all chemical components either decreased or remained stable, except for nitrates, which slightly increased. Notably, a small peak in nitrate mass concentration was observed from 2000 to 2100 UTC, corresponding mainly to the shift in wind direction and the increase in wind speed, suggesting that the primary influencing factor was the alteration of the pollution transport pathway.

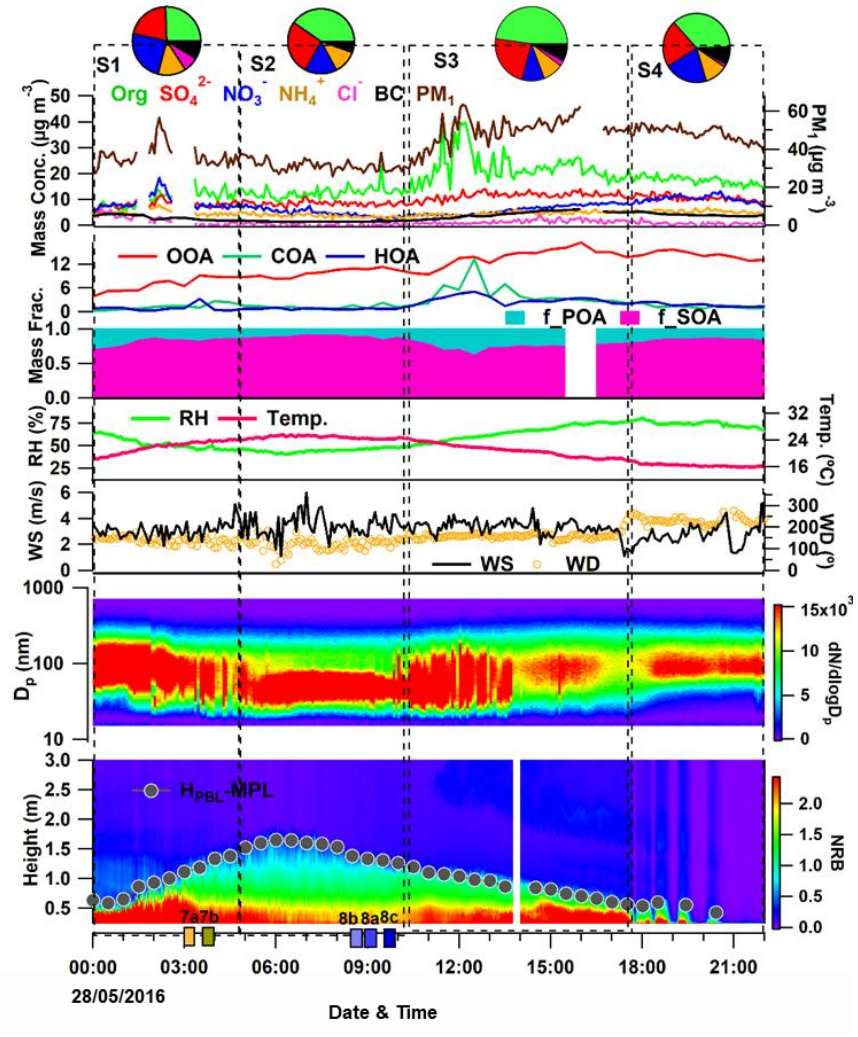

Fig. 3. Time series of (from top to bottom) ground-level concentrations of aerosol chemical components, source apportionment of organic matter, meteorological elements, particle number concentrations, and normalized relative lidar backscatter (NRB) observations derived from the micropulse lidar (grey dots show boundary-layer heights) on 28 May 2016. Time of vertical spirals over Xingtai from RF7 and RF8 are labeled as 7a/b and 8a/b/c. Vertical dashed lines cutting through all panels represent the division of each stage (S1−S4).

3.2 Aircraft-based observations of optical properties

The formation mechanisms of pollution can be considered from two aspects. One is the chemical reactions of internal factors, such as the formation of secondary aerosols, and the other is the impact of boundary-layer development on pollution, i.e., the external environment associated meteorological conditions for pollution [Sun et al., 2018]. During the RF7b (0400 UTC) airborne sub-mission over Xingtai, the vertical distribution of the extinction coefficient clearly shows a pollution profile, with the maximum exceeding 300 M m^{-1} throughout the entire layer (Fig. 4). The wind profile (Fig. 5) reveals that from the near-surface up to 850 hPa (1500 m), southerly winds prevailed, with low wind speeds (< 4 m s^{-1}) and relative humidity levels of 50% to 60%, all favoring the development of air pollutants. Under the combined effects of terrain, emissions, and meteorological factors, the persistent southerly winds in a weak pressure field constitute a typical weather background for pollution formation in the North China Plain [Sun et al., 2018]. Near the surface at that time, Xingtai was located between two high-pressure systems, which led to weak pressure gradients and horizontal diffusion. Thus, the visibility ranged from 18 km to 20 km. There was no obvious inversion in the atmosphere. At 500 hPa, a cyclone positioned over eastern Inner Mongolia guided weak cold air southward. By 0200 UTC, the southern edge of the cold air had reached northern Hebei, but Xingtai was still under stagnant atmospheric conditions. Additionally, the formation of a convergence line before the arrival of cold air further contributed to pollutant accumulation in Xingtai. At around 0900 UTC (RF8), the pressure gradient at 500 hPa gradually increased as the cold vortex began to affect the Xingtai region. However, the weather system was manifested as a forward-tilting trough structure, with the wind direction shifting to northeasterly and wind speed increasing above 850 hPa. The weak cold air (northwesterly wind) primarily impacted areas above 1250 m, while southeasterly wind still prevailed below this level, with a slight increase in wind speed (including near the ground). Consistent with MPL

observations, the vertical atmosphere in the aircraft profile from RF7 (stage S1) to RF8 (stage S2) showed a transition from polluted to clean conditions, with a notable reduction in aerosol extinction. Note that the degree of reduction in the extinction coefficient varied considerably across different altitudes.

The RF8 temperature profile showed a pronounced inversion layer from 1100 m to 1250 m, with a maximum inversion strength of 0.02°C m^{-1}. Assuming that the heating rate of BC absorption in a given layer is roughly proportional to the radiation reaching that layer, the BC heating rate between 1000–1250 m was estimated to be 0.049°C h^{-1} based on the BC distribution during RF8a. This estimation was made using the method proposed by Lu et al. [2020]. Assuming that the maximum heating duration of BC absorption is 4 hours, the maximum temperature increases in this layer due to BC heating was estimated to be 0.20°C. The maximum inversion strength during RF8 was 0.94°C m^{-1}, with warming due to BC heating accounting for ~21.3% of this inversion. Consequently, warm air mass activities contributed to ~78.7% of the inversion at this altitude. The presence of the temperature inversion facilitated the accumulation of pollutants such as BC at this altitude [Deng et al., 2016; Han et al., 2017]. The accumulation of BC, in turn, promoted the development of the inversion layer, indicating a bidirectional positive feedback effect. Due to the inversion layer, the area with large values of extinction coefficient was also concentrated in this layer. For instance, at an altitude of 1120 m, the extinction coefficient was 186.5 M m^{-1} during RF7b and 184.8 M m^{-1} during RF8a, indicating no noticeable decrease in the extinction coefficient.

Under the influence of cold air aloft, the relative humidity above the inversion layer at 1250 m during RF8a dramatically decreased. However, below the top of the inversion layer, particularly within the inversion layer, there was no remarkable decrease in water vapor content. This situation would still be conducive to the hygroscopic growth of particles and liquid-phase chemical reactions, thereby inhibiting the reduction of pollutant concentrations. Within the 1250–1500 m altitude layer above the inversion layer, the extinction coefficient decreased considerably from RF7b to RF8a due to the disturbance caused by weak cold-air activities, with the average extinction coefficient dropping from approximately 190 M m^{-1} to 19 M m^{-1}. Below the inversion layer, there was no obvious cold-air influence, and the southeasterly wind was still the prevailing wind direction. Note

312 that observations were unavailable below 500 m in RF8a, so the 180–500 m layer was not
313 included in the analysis. On the one hand, the slight increase in wind speed at this altitude
314 slightly enhanced the horizontal diffusion of pollutants. On the other hand, the notable
315 differences in the chemical composition of near-surface PM_1 compared with RF7 (stage
316 S1) and the fluctuations in wind direction (Fig. 3) may have caused a shift in the air mass
317 direction during RF8 (stage S2). The section discussing the backward trajectory analysis
318 will examine this further. As a result of these combined effects, there was also a certain
319 decreasing trend in pollutant concentrations, but the decreasing rate was lower than that in
320 the 1250–1500 m layer affected by weak cold-air activities. Specifically, in the 500–950-
321 m altitude range, the aircraft-measured extinction coefficient decreased from ~271 M m^{-1}
322 to 150 M m^{-1}, while the ground-based observations showed a decrease in the extinction
323 coefficient from 140.1 M m^{-1} to 84.9 M m^{-1}.
324 Table 1 presents the mean aerosol optical depth (AOD) values for different layers of the
325 atmosphere over Xingtai during the five flights from RF7a to RF8c, calculated by
326 integrating extinction coefficients over height [Wang et al., 2018]. Due to the influence of
327 the PBL, AOD values greater than 0.1 were mainly found within the boundary layer below
328 2000 m. Overall AOD values recorded during RF7a and RF7b both exceeded 0.3, with
329 values of 0.16 and 0.18 in the 0–1000 m layer, respectively, contributing over 53% to the
330 overall AOD. During RF8, the overall AOD value was noticeably lower compared with
331 RF7, with an average decrease of ~51%. The single-scattering albedo, defined as the ratio
332 of the scattering coefficient to the total extinction coefficient at a specific wavelength
333 [Wang et al., 2018a], also varied. As the atmosphere transitioned from polluted (RF7) to
334 relatively clean (RF8) conditions, the single-scattering albedo within the altitude range of
335 1250–1800 m decreased. Specifically, the average single-scattering albedo in this layer
336 dropped from 0.85 during RF7 to 0.43 during RF8, indicating a prominent increase in the
337 contribution of aerosol absorption to total radiation in the altitude range of 1250–1800 m.
338 Correspondingly, the concentration of BC aerosols also increased markedly in this layer.
339 The bottom of the PBLH is defined as the point where the mean decreasing rate of the
340 aerosol scattering coefficient from aircraft measurements reaches ~0.81 M m^{-1} [F. Wang
341 et al., 2018a]. PBLHs during RF7b and RF8a were thus identified as 1280 m and 1211 m,
342 respectively. However, PBLHs determined by the MPL wavelet method were 1333 m and

1288 m, respectively (Fig. 3). Although the PBLH estimates obtained from the wavelet method are relatively close to aircraft observations, they are slightly overestimated. Due to the pronounced diurnal cycles of the PBL, the airborne-derived PBLH in RF7b (0200 UTC) was higher than that in RF8a (0900 UTC), as shown in Fig. 4. During heavy pollution episodes, the PBLH and meteorological conditions in the PBL play a vital role in the cumulative explosive growth and diffusion of pollutants. High aerosol concentrations can enhance the stability of the urban PBL, thereby lowering the PBLH and further exacerbating pollution, which is known as the "two-way feedback mechanism" [Ding et al., 2016; Liu et al., 2019]. As the atmosphere gradually became cleaner after 0900 UTC, the changing meteorological conditions and the weakening feedback mechanism of pollutants on the PBLH notably slowed down the decreasing rate of the PBLH caused by the diurnal cycle (Fig. 3).

The wind field represents the characteristics of dynamic factors within the PBL. As shown in the wind profiler radar chart (Fig. 5), after entering stage S3 at 1000 UTC, the upper-level cold air continued to descend, reaching an altitude of ~900 m around 1300 UTC. This altitude was also the lowest level of this weak cold-air intrusion. Above 900 m, atmospheric diffusion conditions improved under the influence of the northerly wind. However, below 900 m, the southerly wind still prevailed during stage S3. After 1000 UTC, the near-surface wind speed gradually decreased, and the PBLH further decreased, causing pollutants to accumulate once again.

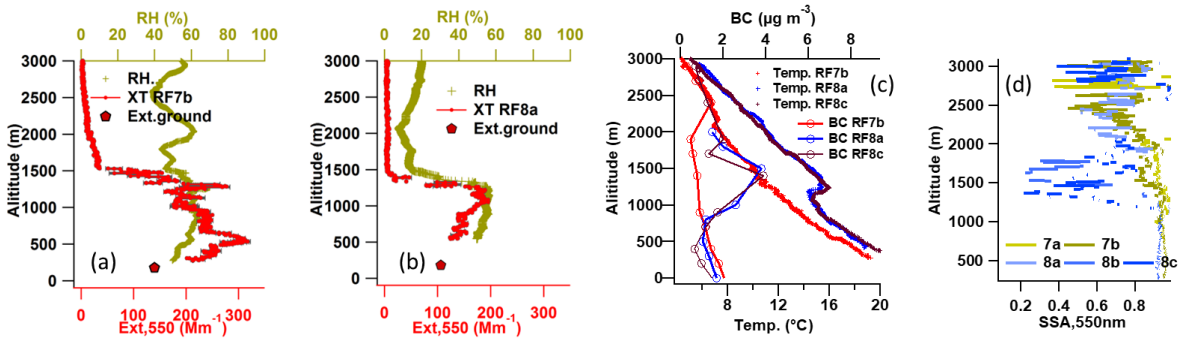

Fig. 4. Vertical distributions of the extinction coefficient and relative humidity during (a) RF7b and (b) RF8a, (c) vertical distributions of the black carbon (BC) concentration and temperature during RF7b, RF8a, and RF8c, and (d) the vertical distribution of the single-scattering albedo during the RF7 and RF8 flights.

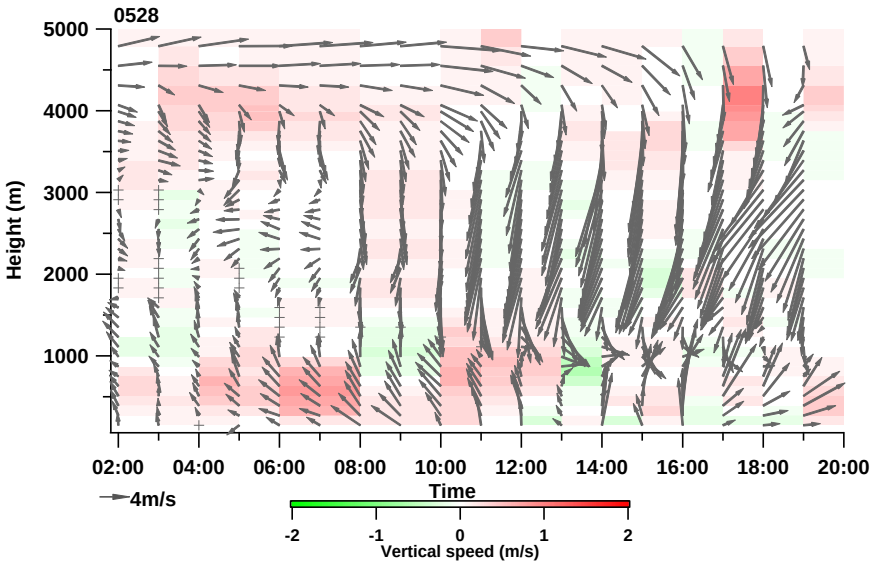

Fig. 5. Vertical wind field measured by a wind profiler radar near Xingtai on 28 May 2016.

Table 1. Mean aerosol optical depths in different layers above Xingtai during the RF7 and RF8 flights.

Flights	Aerosol optical depths			
	0–1000 m	1000–2000 m	2000–3000 m	3000–4000 m
RF7a	0.16	0.14	6.23×10^{-3}	n/a
RF7b	0.18	0.15	6.81×10^{-3}	4.10×10^{-4}
RF8a	0.07	0.06	4.80×10^{-3}	2.22×10^{-4}
RF8b	0.11	0.07	n/a	n/a
RF8c	0.10	0.05	3.32×10^{-3}	5.09×10^{-4}

3.3 Air mass trajectory analysis

The 72-hour backward trajectories of air masses from 0000 UTC to 2300 UTC on 28 May 2016 were analyzed (Fig. 6). Results reveal a shift in the direction of air masses at an altitude of 200 m between stages S2 (RF8) and S1 (RF7). During stage S2, the air masses veered easterly, originating from the heavily polluted areas of eastern Hebei and northwestern Shandong. After passing over the sea, the air masses traveled through Jiangsu, Anhui, and Henan before reaching Xingtai. The water vapor contents of the air masses increased during this journey. Compared with stage S1, the air masses during stage S2 moved noticeably faster, corresponding to a slight increase in surface wind speed during this period. In stage S2, the direction of the air masses changed, and the faster movement of air masses improved atmospheric diffusion, resulting in a slight decrease in near-surface pollutant concentrations compared with stage S1. In stage S3, the movement of air masses

slowed down again, with a direction similar to that in stage S1, leading to further pollution accumulation. During stage S4, at an altitude of 200 m, there was a pronounced adjustment in the direction of pollutant transport. Specifically, air masses originated from Henan in the southwest direction, and the relative humidity of these air masses was relatively high, facilitating the continued development of pollution. At an altitude of 1000 m within the PBL, the air masses consistently came from the southeast across all periods, with no marked difference in pollution sources between stages S1 and S2. However, at an altitude of 2000 m above the PBL, the air mass direction in stage S1 showed no notable difference from that at lower altitudes. By contrast, during stage S2, the air masses came from the relatively clean northwestern region and moved faster, leading to a cleaner atmosphere at higher altitudes.

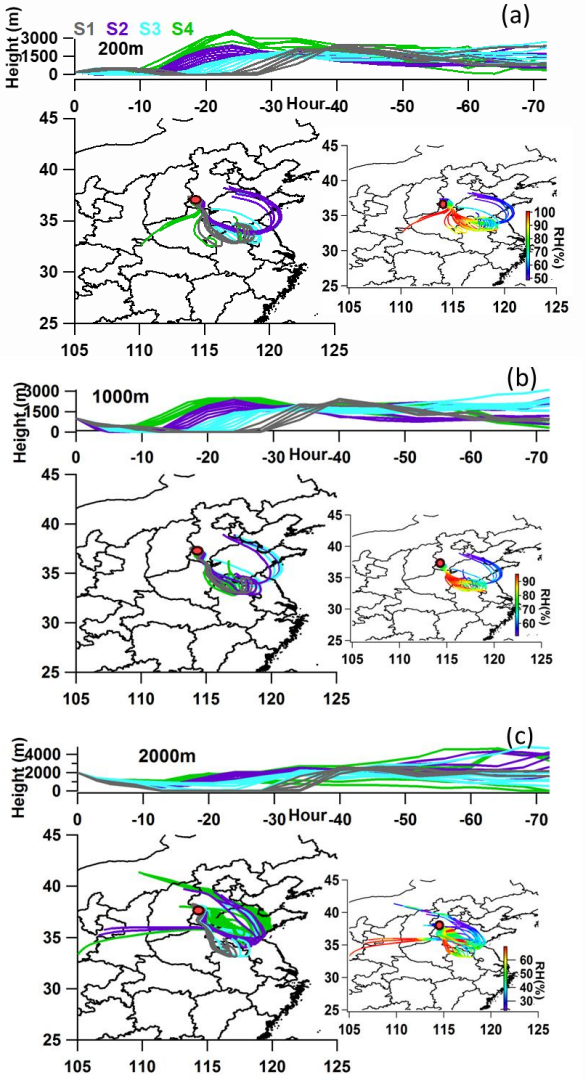

Fig. 6. Seventy-two-hour backward trajectories at altitudes of (a) 200 m, (b) 1000 m, and (c) 2000 m from 0000 UTC to 2300 UTC on 28 May 2016. The upper figures in panels (a–c) show 72-hour backward trajectory height maps of S1-S4, the lower left figures show the origins of the backward trajectories of S1–S4, and the lower right figures show the relative humidity (unit: %) of trajectories from different origins.

3.4 Aircraft-based observations of pollutant gases

As showed in Fig.7, consistent with the changes in the extinction coefficient, the concentrations of various pollutants (including SO_2, NO_2, and CO) in RF8 were noticeably lower than those in RF7, primarily concentrated below 1500 m. Above 1500 m, the concentrations of these pollutants quickly dropped to lower values as the background of the free troposphere. The trend for O_3 was the opposite. Below 1500 m, the O_3 concentration in RF8 was higher than that in RF7. Between 1500 m and 2300 m, the O_3 concentration rapidly decreased from above 110 μg m^{-3} to ~75–82 μg m^{-3}, lower than the O_3 concentration at the same altitude in RF7. Above 2300 m, there was little difference in the O_3 concentration between RF7 and RF8. Notably, the O_3 profile in RF7 did not rapidly decrease at any particular altitude, remaining in the range of ~80 to 102 μg m^{-3} throughout the entire layer.

Gaseous and particulate pollutants from power plants, industrial emissions, and transportation contribute substantially to atmospheric extinction in the vertical direction. The correlations between pollutant gases and extinction (Figs. 8 and 9) reveal that in RF7 (representing a relatively polluted atmospheric background), SO_2, NO_2, and CO concentrations were strongly correlated with the scattering coefficient. The correlation coefficients(R^2) of SO_2 and NO_2 with the scattering coefficient were particularly high, reaching 0.92 and 0.96, respectively. However, in RF8 (representing a relatively clean atmosphere), these correlations decreased markedly. However, SO_2 was still highly correlated with the scattering coefficient (coefficient of determination, $R^2 = 0.88$). Unlike other pollutants, the correlation between O_3 and the scattering coefficient in RF7 differed depending on the PBLH observed during the flight (with an average PBLH of 1211 m). Above the boundary layer (PBLH > 1211 m), O_3 was positively correlated with the scattering coefficient ($R^2 = 0.86$), with the corresponding scattering coefficients mainly ranging from 0 to 100 M m^{-1}. This suggests that in the upper atmosphere, where the influence of the boundary layer is reduced, the O_3 concentration and atmospheric scattering

properties were closely linked, potentially due to photochemical reactions and transport processes affecting both O_3 and particulate matter. However, within the boundary layer (PBLH $\leq$ 1211 m) in RF7, as the scattering coefficient increased, the O_3 concentration gradually decreased. By contrast, in the relatively clean atmosphere in RF8, the O_3 concentration and the scattering coefficient showed a consistent positive correlation (R^2 = 0.90), even higher than the correlations between other gases and the scattering coefficient during RF8. It shows O_3 and $PM_{2.5}$ (both secondary pollutants) are formed from the same emissions.

In RF7, O_3 generally contributed positively to extinction at relative humidity levels below 50%. However, when the relative humidity exceeded 50%, the contribution of O_3 to extinction was either positive or negative. In RF8, a similar pattern was seen, with 50% relative humidity serving as the threshold. Below this threshold, an increase in relative humidity favored O_3 formation, leading to a higher O_3 concentration and a corresponding rise in the scattering coefficient. Nevertheless, when the relative humidity exceeded 50%, the O_3 concentration tended to fall in the 105–125 μg m^{-3} range. There was no apparent correlation of O_3 and the scattering coefficient with relative humidity.

NO_2 and CO can be regarded as tracers for O_3 pollution [Kim et al., 2013]. NO_2 has a relatively short lifespan and primarily influences O_3 through photochemical reactions. The RF7 flight occurred in the morning (Beijing time), and solar ultraviolet radiation during this period is generally notably weaker compared with noon and the afternoon hours. Atmospheric pollution within the boundary layer also further weakens the amount of solar ultraviolet radiation to some extent, inhibiting the photochemical cycle of O_3 formation, thereby leading to the reduction and consumption of O_3. This phenomenon is known as the titration effect. This is seen during the RF7 and RF8 flights, i.e., a decrease in the O_3 concentration accompanied by an increase in the NO_2 concentration (Fig. 9). Due to the strong correlation between NO_2 and the scattering coefficient, the extinction coefficient also showed a noticeable upward trend. CO is another important precursor of tropospheric O_3. Above the boundary layer, where nitrogen oxide concentrations are lower, and titration reactions are weaker, O_3 was not noticeably consumed. This maintained the relatively high O_3 concentration above the boundary layer, where the CO mass concentration in RF7 was also notably higher than that in RF8. During RF8, due to the influence of weak cold-air

activities, the concentrations of all pollutants within the boundary layer, except for O_3, decreased compared with RF7. The main reason for this may be that the RF8 flight took place in the afternoon (Beijing time) when sunlight was stronger. The atmosphere during RF8 was cleaner than that during RF7, leading to a marked reduction in the atmospheric extinction capacity of pollutants. At this time, enhanced solar radiation, particularly the intense ultraviolet radiation, intensified the photochemical cycling of nitrogen oxides, thereby actively promoting O_3 formation. Consequently, within the boundary layer, a positive correlation between O_3 and the scattering coefficient was found. Above the boundary layer, due to the influence of weak cold-air activities, the concentrations of O_3 and other gaseous pollutants decreased to relatively lower levels. However, the correlation exhibited by different gases and extinction may involve complex physicochemical mechanisms, and further corroboration with a large amount of sample data is still required.

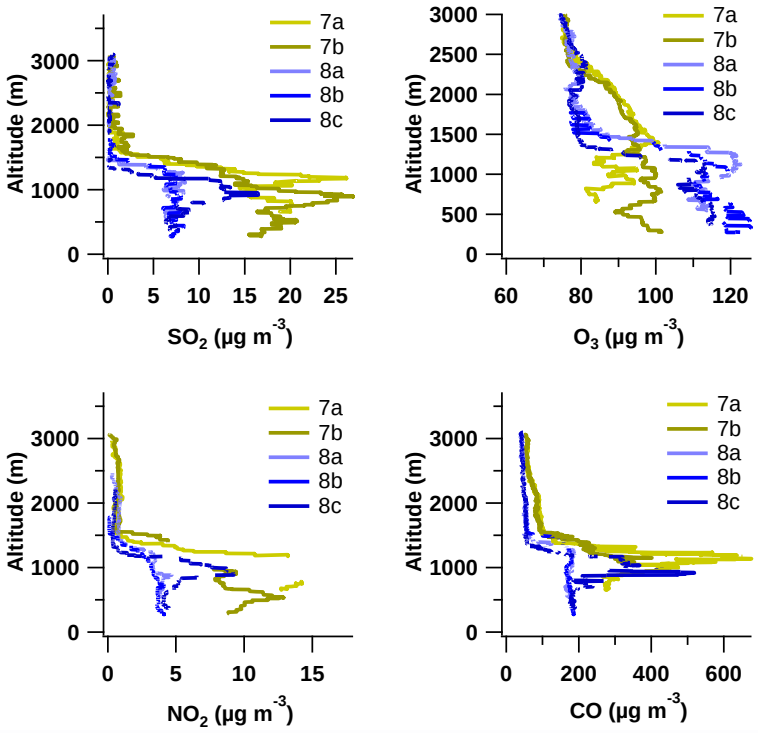

Fig. 7. Vertical profile distributions of SO_2, O_3, NO_2, and CO concentrations during the RF7 and RF8 flights.

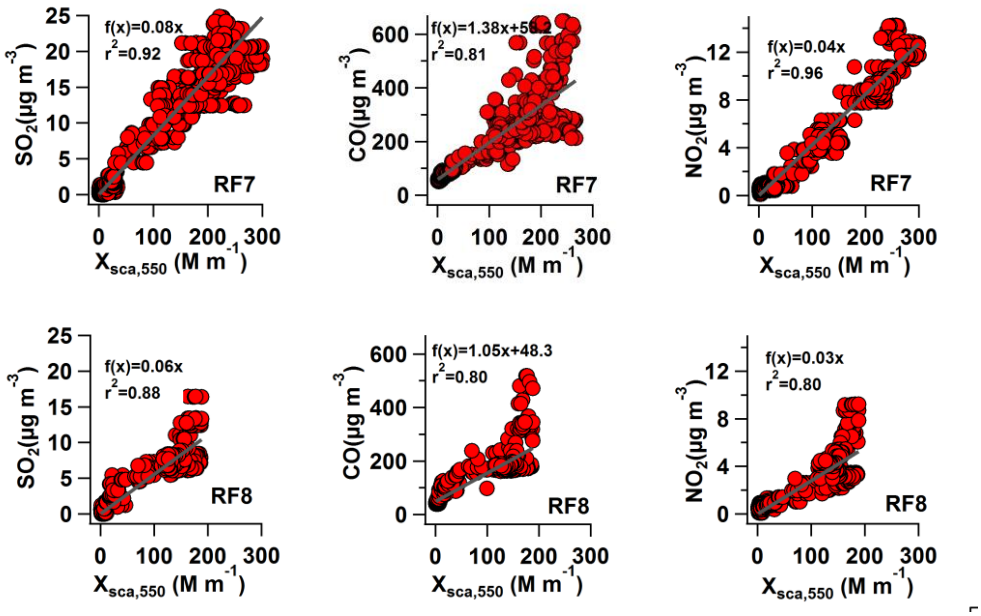

Fig. 8. Correlations of SO_2, NO_2, and CO concentrations with the scattering coefficient during the RF7 (top row) and RF8 (bottom row) flights.

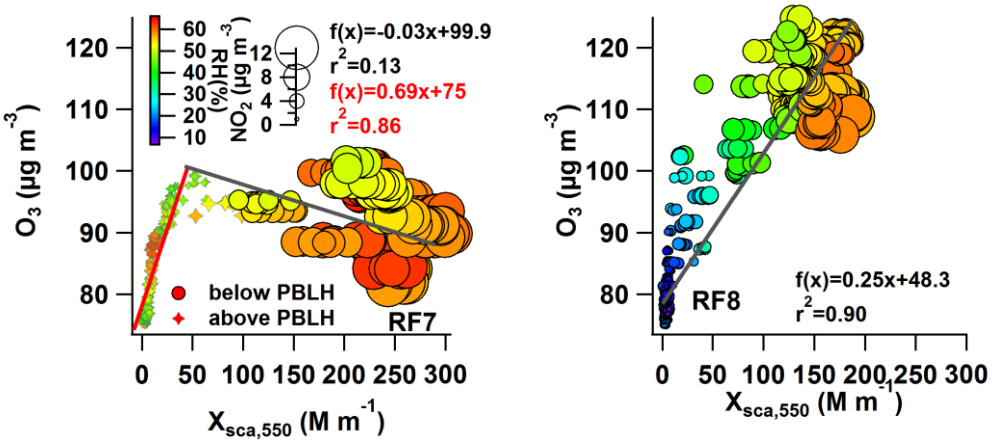

Fig. 9. Correlations between the O_3 concentration and the scattering coefficient during the RF7 and RF8 flights. The circle color and size denote the relative humidity and the NO_2 concentration, respectively.

4 Conclusions

Air pollution remains a significant environmental issue in China, especially in the Beijing-Tianjin-Hebei region. Within the boundary layer, various meteorological elements and multiple boundary-layer components are complex and highly variable, playing a crucial role in the formation and dissipation of pollution. Detailed observations within the boundary layer are essential for accurately capturing the thermal and dynamic evolution of boundary-layer structures during pollution processes, which in turn enhances our

understanding of the pollution mechanisms in the Beijing-Tianjin-Hebei region. The factors influencing pollution development can be categorized into two aspects. One involves the reactions related to the physicochemical properties of pollutants, such as the formation of secondary aerosols. The other concerns the impact of external environmental factors, such as the role of boundary-layer structures in pollution processes. In this study, based on aircraft observations from Xingtai in Hebei made in May 2016, combined with ground-level multi-source data, including PM_1 chemical composition, we investigate aerosol composition and optical properties, vertical pollution characteristics of gases within the boundary layer, and their interactions with meteorological parameters. Special emphasis is placed on exploring the transport and evolution mechanisms of a pollution-to-clean transition (RF7–RF8) in the Xingtai region during the summer.

From ground-level observations, the overall PM_1 mass concentration in stage S1 (RF7) was relatively low at 37.5 μg m^{-3}, and the contribution of inorganic salts was considerably greater than that of organics. Upon entering stage S2 (RF8), the near-surface wind speed slightly increased, and the wind direction fluctuated to some extent, but the prevailing wind direction remained southeasterly. During stage S2, the thickness of the pollution layer noticeably decreased, and pollutant concentrations showed distinct weakening trends in the vertical direction. Although the average ground-level PM_1 mass concentration (30.6 μg m^{-3}) slightly decreased, the chemical composition of PM_1 during stage S2 differed markedly from that during stage S1. The contribution of nitrates decreased to around 16%, while the proportion of organics gradually increased to about 40%. The contribution of secondary organic aerosols (over 90%) was greater than that of the organics. Aircraft observations revealed that at ~0900 UTC (RF8), the pressure gradient at 500 hPa gradually increased as a cold vortex began to influence the Xingtai region. The primary impact of weak cold-air activities was observed above 1250 m, while below this height, the prevailing wind direction remained southeasterly, and the wind speed increased. From RF7 (stage S1) to RF8 (stage S2), the vertical atmosphere gradually transitioned from polluted to clean. In RF8, the temperature profile had a pronounced inversion at an altitude of approximately 1100–1250 m, with a maximum inversion strength of 0.94°C m^{-1}. The warming from BC heating contributed about 21.3% of this inversion. The presence of the inversion facilitated

pollutant accumulation, and the BC accumulation further promoted the development of the inversion layer, indicating a bidirectional positive feedback effect between the two. The backward trajectory analysis shows that air masses at both 2000 m and 1000 m during stage S1 came from the southeast direction. However, during stage S2, the air masses at 2000 m shifted toward the cleaner northwestern region compared with those at the same height in stage S1, moving at a faster speed, which corresponds to the transition of the upper atmosphere to a cleaner state.

In RF7, SO_2, NO_2, and CO concentrations were strongly correlated with the scattering coefficient, with correlation coefficients of 0.92 and 0.96 for SO_2 and NO_2, respectively. However, in RF8, these correlations dramatically decreased. However, the SO_2 concentration was still relatively highly correlated with the scattering coefficient (R^2 = 0.88). From RF7 to RF8, the concentrations of all pollutants within the boundary layer, except for O_3, had decreasing trends. Within the boundary layer, O_3 concentrations gradually decreased as the scattering coefficient increased. Above the boundary layer, the O_3 concentration was positively correlated with the scattering coefficient (R^2 = 0.86), with corresponding scattering coefficients mainly ranging from 0 to 100 M m^{-1}. Whether under clean (RF8) or polluted (RF7) weather conditions, O_3 generally contributed positively to extinction when the relative humidity was below 50%. However, when the relative humidity exceeded 50%, the contribution of O_3 to extinction was either positive or negative. There was no apparent correlation of O_3 and the scattering coefficient with relative humidity.

Acknowledgements. The authors greatly appreciate the research team and the flight crew of the Hebei Weather Modification Center for their participation in the experiment. We also acknowledge support from the CMA Key Innovation Team (CMA2022ZD10) and the WMC Innovation Team (WMC2023IT03). The reviewers are also gratefully acknowledged for their constructive comments.

References

Benish SE, He H, Ren X, Roberts SJ, Salawitch R J, Li Z, Wang F, Wang Y, Zhang F, Shao M, Lu S, Dickerson RR (2020) Measurement report: aircraft observations of ozone, nitrogen oxides, and volatile organic compounds over Hebei Province, China. Atmos Chem Phys 20, 14,523–14,545, https://doi.org/10.5194/acp-20-14523-2020

Brook JR, Makar PA, Sills DML, Hayden KL, McLaren R (2013) Exploring the nature of air quality over

550 southwestern Ontario: main findings from the Border Air Quality and Meteorology Study. Atmos Chem
551 Phys 13, 10,461–10,482, https://doi.org/10.5194/acp-13-10461-2013
552 Cai W, Xu X, Cheng X, Wei F, Qiu X, Zhu W (2020) Impact of "blocking" structure in the troposphere on
553 the wintertime persistent heavy air pollution in northern China. Sci Total Environ 741, 140325,
554 https://doi.org/10.1016/j.scitotenv.2020.140325
555 Deng H, Tan H, Li F, Cai M, Chan P W, Xu H, Huang X, Wu D (2016) Impact of relative humidity on
556 visibility degradation during a haze event: a case study. Sci Total Environ 569–570, 1149–1158
557 Ding A J, Huang X, Nie W, Sun JN, Kerminen VM, Petäjä T, Su H, Cheng Y F, Yang X Q, Wang MH.
558 (2016) Enhanced haze pollution by black carbon in megacities in China. Geophys Res Lett 43(6), 2873–
559 2879
560 Ding G, Chan C, Gao Z, Yao W, Li Y, Cheng X, Meng Z, Yu H, Wong K, Wang S, Miao Q. (2005) Vertical
561 structures of PM_{10} and $PM_{2.5}$ and their dynamical character in low atmosphere in Beijing urban areas.
562 Sci China Earth Sci 48, 38–54
563 Dong Z, Li Z, Yu X, Cribb M, Li X, Dai J. (2017) Opposite long-term trends in aerosols between low and
564 high altitudes: a testimony to the aerosol–PBL feedback. Atmos Chem Phys 17(12), 7997–8009,
565 https://doi.org/10.5194/acp-17-7997-2017
566 Drinovec L, Močnik G, Zotter P, Prévôt ASH, Ruckstuhl C, Coz E, Rupakheti M, Sciare J, Müller T,
567 Wiedensohler A, Hansen ADA. (2015) The "dual-spot" Aethalometer: an improved measurement of
568 aerosol black carbon with real-time loading compensation. Atmos Meas Tech 8, 1965–1979,
569 https://doi.org/10.5194/amt-8-1965-2015
570 Friedrich K, Lundquist JK, Aitken M, Kalina EA, Marshall RF (2012) Stability and turbulence in the
571 atmospheric boundary layer: a comparison of remote sensing and tower observations. Geophys Res Lett
572 39(3), https://doi.org/10.1029/2011GL050413
573 Gamage N, Hagelberg C (1993) Detection and analysis of microfronts and associated coherent events using
574 localized transforms. J. Atmos. Sci 50(5), 750–756
575 Han S, Hao T, Zhang Y, Liu J, Li P, Cai Z, Zhang M, Wang Q, Zhang H (2017) Vertical observation and
576 analysis on rapid formation and evolutionary mechanisms of a prolonged haze episode over central-
577 eastern China. Sci Total Environ 616–617, 135–146
578 Han S, Hao T, Zhang Y, Liu J, Li P, Cai Z, Zhang M, Wang Q, Zhang H (2018) Vertical observation and
579 analysis on rapid formation and evolutionary mechanisms of a prolonged haze episode over central-
580 eastern China, Sci Total Environ 616–617, 135–146, https://doi.org/10.1016/j.scitotenv.2017.10.278
581 Haskins J D, Lee B H, Lopez-Hilifiker F D, Peng Q, Jaeglé L, Reeves J M (2019) Observational constraints
582 on the formation of Cl_2 from the reactive uptake of $ClNO_2$ on aerosols in the polluted marine boundary
583 layer. J Geophys Res-atmos 124, 8851–8869, https://doi.org/10.1029/2019JD030627
584 Jiang Q, Sun Y, Wang Z, Yin Y (2014) Aerosol composition and sources during the Chinese Spring Festival:
585 fireworks, secondary aerosol, and holiday effects. Atmos Chem Phys 14(14), 20,617–20,646
586 Jiang Y, Xin J, Zhao D, Jia D, Tang G, Quan J, Wang M, Dai L (2021) Analysis of differences between

thermodynamic and material boundary layer structure: comparison of detection by ceilometer and microwave radiometer. Atmos Res 248, 105179, https://doi.org/10.1016/j.atmosres.2020.105179

Kim PS, Jacob DJ, Liu X, Warner JX, Yang K, Chance K, Thouret V, Nedelec P (2013) Global ozone–CO correlations from OMI and AIRS: constraints on tropospheric ozone sources. Atmos Chem Phys 13, 9321–9335, https://doi.org/10.5194/acp-13-9321-2013

Levin EJT, Kreidenweis SM, McMeeking GR, Carrico CM, Collett JL, Malm WC (2009) Aerosol physical, chemical and optical properties during the Rocky Mountain Airborne Nitrogen and Sulfur study. Atmos Environ 43(11), 1932–1939, https://doi.org/10.1016/j.atmosenv.2008.12.042

Li X, Quan JL, Wang F, Sheng J, Gao Y, Zhao D, Cheng Z (2018) Evaluation of the method for planetary boundary layer height retrieval by lidar and its application in Beijing. Chinese J Atmos Sci (in Chinese) 42(2), 435−446, https://doi.org/10.3878/j.issn.1006-9895.1710.17173

Liu L, Zhang X, Zhong J, Wang J, Yang Y (2019) The 'two-way feedback mechanism' between unfavorable meteorological conditions and cumulative $PM_{2.5}$ mass existing in polluted areas south of Beijing. Atmos Environ 208, 1−9, https://doi.org/10.1016/j.atmosenv.2019.02.050

Lu Q, Liu C, Zhao D, Zeng C, Li J, Lu C, Wang J, Zhu B (2020) Atmospheric heating rate due to black carbon aerosols: uncertainties and impact factors. Atmos Res 240, 104891, https://doi.org/10.1016/j.atmosres.2020.104891

Pusede SE, Duffey KC, Shusterman AA, Saleh A, Laughner JL., Wooldridge PJ, Zhang Q, Parworth CL, Kim H, Capps SL, Valin LC, Cappa CD, Fried A, Walega J, Nowak JB, Weinheimer AJ, Hoff RM, Berkoff TA, Beyersdorf AJ, Olson J, Crawford JH, Cohen RC (2016) On the effectiveness of nitrogen oxide reductions as a control over ammonium nitrate aerosol. Atmos Chem Phys 16(4), 2575−2596, https://doi.org/10.5194/acp-16-2575-2016

Qu Y, Han Y, Wu Y, Gao P, Wang T (2017) Study of PBLH and its correlation with particulate matter from one-year observation over Nanjing, Southeast China. Remote Sens 9(7), 668, https://doi.org/10.3390/rs9070668

Ren H, Hu W, Wei L, Yue S, Zhao J, Li L, Wu L, Zhao W, Ren L, Kang M, Xie Q, Su S, Pan X, Wang Z, Sun Y, Kawamura K, Fu P (2021) Measurement report: vertical distribution of biogenic and anthropogenic secondary organic aerosols in the urban boundary layer over Beijing during late summer. Atmos Chem Phys 21(17), 12,949−12,963, https://doi.org/10.5194/acp-21-12949-2021

Riedel TW, Nicholas DW, Dubé WP, Middlebrook AM, Young Cora J, Öztürk F, Bahreini Roya, VandenBoer TC, Dan W, Williams EJ, Roberts JM, Steven B, and Thornton AJ (2013) Chlorine activation within urban or power plant plumes: vertically resolved $ClNO_2$ and Cl_2 measurements from a tall tower in a polluted continental setting. J Geophys Res-atmos 118(15), 8702−8715, https://doi.org/10.1002/jgrd.50637

Sun P, Nie W, Chi X, Xie Y, Huang X, Xu Z, Qi X, Xu Z, Wang L, Wang T, Zhang Q, Ding A (2018) Two years of online measurement of fine particulate nitrate in the western Yangtze River Delta: influences of thermodynamics and N_2O_5 hydrolysis. Atmos Chem Phys 18(23), 17,177−17,190,

https://doi.org/10.5194/acp-18-17177-2018

Sun P, Nie W, Wang T, Chi X, Huang X, Xu Z, Zhu C, Wang L, Qi X, Zhang Q, Ding A (2020) Impact of air transport and secondary formation on haze pollution in the Yangtze River Delta: in situ online observations in Shanghai and Nanjing. Atmos Environ 225, 117350, https://doi.org/10.1016/j.atmosenv.2020.117350

Sun Y, Jiang Q, Xu Y, Ma Y, Zhang Y, Liu X, Li W, Wang F, Li J, Wang P, Li Z (2016a) Aerosol characterization over the North China Plain: haze life cycle and biomass burning impacts in summer. J Geophys Res-atmos 121, 2508−2521, https://doi.org/10.1002/2015JD024261

Sun Y, Wei D, Fu P, Wang Q, Jie L, Ge X, Qi Z, Zhu C, Ren L, Xu W (2016b) Primary and secondary aerosols in Beijing in winter: sources, variations and processes. Atmos Chem Phys 16(13), 1−41, https://doi.org/10.5194/acp-16-8309-2016

Sun Y, Lei L, Zhou W, Chen C, He Y, Sun J, Li Z, Xu W, Wang Q, Ji D, Fu P, Wang Z, Worsnop DR (2020) A chemical cocktail during the COVID-19 outbreak in Beijing, China: insights from six-year aerosol particle composition measurements during the Chinese New Year holiday. Sci Total Environ 742, 140739, https://doi.org/10.1016/j.scitotenv.2020.140739

Wang F, Li Z, Ren X, Jiang Q, He H, Dickerson RR, Dong X, Lv F (2018) Vertical distributions of aerosol optical properties during the spring 2016 ARIAs airborne campaign in the North China Plain. Atmos Chem Phys 18, 8995–9010, https://doi.org/10.5194/acp-18-8995-2018

Wang F, Li Z, Jiang Q, Ren X, He H, Tang Y, Dong X, Sun Y, Dickerson RR (2024) Comparative analysis of aerosol vertical characteristics over the North China Plain based on multi-source observation data. Remote Sens, 16(4), 609, https://doi.org/10.3390/rs16040609

Wang Q, Sun Y, Xu W, Du W, Zhou L, Tang G, Chen C, Cheng X, Zhao X, Ji D (2018) Vertically-resolved characteristics of air pollution during two severe winter haze episodes in urban Beijing, China. Atmos Chem Phys 18, 2495–2509, https://doi.org/10.5194/acp-18-2495-2018

Wang Z., Cao X, Zhang L, Notholt J, Zhou B, Liu R, Zhang B (2012) Lidar measurement of planetary boundary layer height and comparison with microwave profiling radiometer observation. Atmos Meas Tech 5(8), 1965–1972, https://doi.org/10.5194/amt-5-1965-2012

Wu Q, Wang Z, Gbaguidi A, Gao C, Li L, Wang W (2011) A numerical study of contributions to air pollution in Beijing during CAREBeijing-2006. Atmos Chem Phys 11, 5997–6011, https://doi.org/ 10.5194/acp-11-5997-2011

Xu X, Cai W, Zhao T, Qiu X, Zhu W, Sun C, Yan P, Wang C, Ge F (2021) “Warm cover”: precursory strong signals for haze pollution hidden in the middle troposphere. Atmos Chem Phys 21(18), 14,131–14,139, https://doi.org/10.5194/acp-21-14131-2021

Zhang Y, Du W, Wang Y, Wang Q, Wang H, Zheng H, Zhang F, Shi H, Bian Y, Han Y, Fu P, Canonaco F, Prévôt ASH, Zhu T, Wang P, Li Z, Sun Y (2018) Aerosol chemistry and particle growth events at an urban downwind site in the North China Plain. Atmos Chem Phys 18, 14,637–14,651,

https://doi.org/10.5194/acp-18-14637-2018

Zhou D, Ding K, Huang X, Liu L, Liu Q, Xu Z, Jiang F, Fu C, Ding A (2018) Transport, mixing and feedback of dust, biomass burning and anthropogenic pollutants in eastern Asia: a case study. Atmos Chem Phys 18(22), 16,345–16,361, https://doi.org/10.5194/acp-18-16345-2018